Current-Voltage Characterization of Charge Injection Transistors Using Predictor-Corrector Continuation

Mark Pinto and Serge Luryi

AT&T Bell Laboratories, Murray Hill, NJ 07974

Introduction

The charge injection transistor or CHINT[1] is a three-terminal heterojunction device which operates on the principle of real-space transfer (RST) of electrons, heated by a lateral field, over an energy barrier. Experimental CHINT *IV* characteristics are extremely nonlinear, including strong negative differential resistance (NDR) and sharp steps (see fig. 1)[2]. Monte Carlo (MC) simulations[3] of the CHINT, demonstrate internal switching and the formation of high-field domains. However both experimental measurements and MC calculations have been limited in analyzing RST effects due to the restriction of tracing *IV* characteristics exclusively in voltage increments.

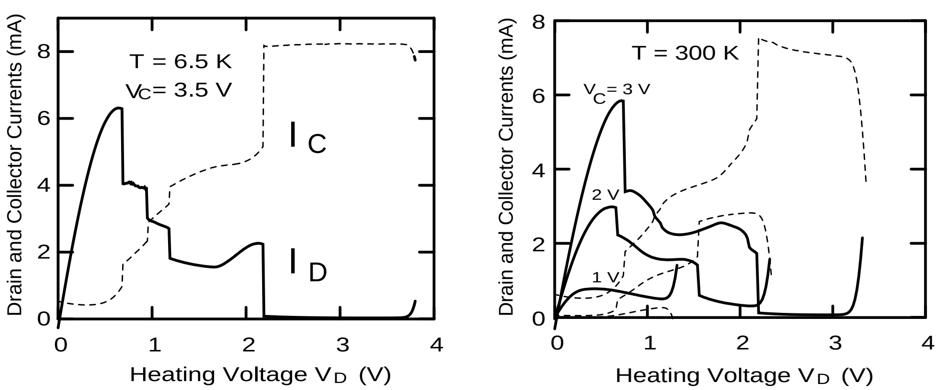

Figure 1:
Experimental InGaAs/InAlAs CHINT *IV* characteristics (a) $T = 6.5$K (b) $T = 300$K.[2]

By using predictor-corrector continuation methods[4], we have been able to trace completely the connected graph components of CHINT *IV* space. As a result, we have discovered a multiplicity of anomalous $V_{DS} = 0$ states and what is believed the first occurrence of *multiply connected, self-intersecting IV curves* in an electronic device[5,6]. Known NDR devices may exhibit multivalued functions in the $I(V)$ dependence (e.g., the *pnpn* diode), in the $V(I)$ dependence (the Esaki tunnel diode, the Gunn diode), or even in both (the thyristor, the resonant tunnel diode in the intrinsic-bistability range) – but these can always be traced as a continuous curve in the (V, I) plane. The loops and folds found in our CHINT simulations provide a qualitative explanation for experimentally observed nonlinearities. Furthermore the understanding gained through complete mapping of operational phase space may lead to new RST device elements.

Before reviewing results obtained on *IV* mappings, mathematical models and algorithms salient to the CHINT analysis are briefly summarized. The InGaAs/InAlAs device structure employed here is described in a companion paper[7] which concentrates on a detailed analysis of domain formation and the anomalous, collector controlled states.

Mathematical model for continuous simulation of real-space transfer

Any model which attempts to account for real-space transfer effects must directly include terms for carrier heating. Further, the ability to specify some form of Neumann boundary conditions is essential for tracing arbitrary, multivalued *IV* characteristics. Both of these requirements can be met by the general-purpose device simulator PADRE[8] which solves partial differential equations derived from moments of the Boltzmann equation. In the following, we have used the energy balance system[9, 10], defined in terms of the electrostatic potential ψ, the electron density n, and the electron temperature T_e as follows:

$$\nabla \cdot (\varepsilon \nabla \psi) = -q\,(p - n + N) \tag{1}$$

$$\frac{\partial n}{\partial t} = \frac{1}{q}\,\nabla \cdot \mathbf{J} \tag{2}$$

$$\nabla \cdot \mathbf{S} = \mathbf{J} \cdot \mathbf{F} - \frac{3k}{2}\, n\, \frac{T_e - T}{\tau_w} - \frac{3k}{2}\,\frac{\partial (n\, T_e)}{\partial t}\ . \tag{3}$$

The electron current density $\mathbf{J}$ and energy flux $\mathbf{S}$ are given by

$$\mathbf{J} = q\,\mu \left[n\,\mathbf{F} + \frac{k}{q}\,\nabla (n\, T_e) \right] \tag{4}$$

$$\mathbf{S} = -\frac{5}{2}\,\frac{k\,T_e}{q}\,\left[\mathbf{J} + \kappa_0\, k\, \mu\, n\, \nabla T_e \right]\ . \tag{5}$$

In (1) – (5), q is the electronic charge, p is the hole density (a function of ψ), k is Boltzmann's constant, ε is the permittivity, μ is the mobility, τ_w is the energy relaxation time, κ_0 is a dimensionless heat conduction coefficient, and F is the carrier driving force, including quasi-fields (i.e., from local band-gap variations).

Through an element-based data structure, PADRE decomposes a device domain into arbitrary, nonplanar configurations of regions; for instance, any number of heterointerfaces can terminate abruptly at a single location (node). Data at the verticies of each element can have local material and model dependencies, e.g. μ, ε, τ_w, and k_0 in (1)-(5). The impurity concentration N and solution variables are allowed to change abruptly across any heterostructure interface. In this analysis, the quasi-Fermi level and T_e are assumed continuous, thus introducing a T_e dependence in the interface condition on local electron density n; for Boltzmann statistics, this condition reduces to

$$n^{(m2)} = n^{(m1)}\,\frac{N_C^{(m2)}}{N_C^{(m1)}}\,\exp\left[-\frac{\Delta E_c(m2 - m1)}{k\,T_e} \right] \tag{6}$$

at an interface between materials $m1$ and $m2$, where ΔE_c is the conduction band offset and N_C represents the density of states. These relations imply that the RST current density at energy barriers is thermionic and included self-consistently.

Models for μ and τ_w as a function of T_e are typically derived from user-defined (e.g. MC) velocity-field $v(F)$ and temperature-field $T_e(F)$ relations for homogeneous slabs. To avoid confusion with negative differential mobility effects arising from momentum space transfer, a single population of electrons has been used here with a monotonic $\mathrm{v}(F) = \mu_0 F[1 + (\mu_0 F/\mathrm{v}_{sat})^2]^{1/2}$ relation[11] together with the $T_e(F)$ implied by a T_e-independent diffusivity[12] and a consistent κ_0[9]. We have checked that our results remain qualitatively similar for more realistic $\mathrm{v}(F)$, $T_e(F)$. For similar reasons, impact ionization and tunneling effects were excluded. Other parameters were selected to match the InGaAs/InAlAs system as exactly as possible. Of critical importance is the barrier height, taken as $\Delta E_c = 0.5\mathrm{eV}$; the low field mobility μ_0 was assumed a function of the local ionized impurity concentration such that $\mu_0 \approx 10^4 \mathrm{cm}^2/\mathrm{V{\cdot}s}$ in the emitter.

In order to trace the complex CHINT *IV* curves shown below, it is necessary to use a mixed current/voltage boundary condition. We have used predictor-corrector continuation[4] based on a pseudo-arclength σ for this purpose. Computationally, the continuation method requires the addition of a single algebraic auxiliary equation, typically written in terms of the voltage and current (V_j, I_j) and the unit tangent $(\dot{V}_j, \dot{I}_j)$ at a known point on the curve j. The unit tangent can also be used to detect limit points (e.g. where $\dot{V}=0$ or $\dot{I}=0$) and to predict an initial guess for the subsequent bias point $j+1$. Fig. 2 illustrates the continuation method and associated auxiliary condition on the pseudo-arclength used here.

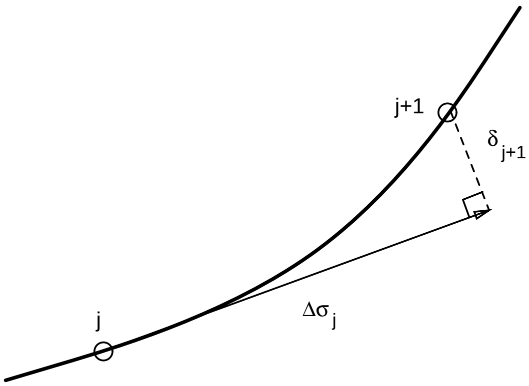

Figure 2:
Predictor-corrector continuation applied to step between consecutive points j and $j+1$ on an *IV* curve. The corresponding auxiliary equation is

$$\dot{I}_j\,(I-I_j) + \dot{V}_j\,(V-V_j) - \Delta\sigma_j \;=\; 0$$

where the next pseudo-arclength step $\Delta\sigma_{j+1}$ is automatically controlled by a user-specified tolerance on the error of the tangential projection δ_j.

DC mappings of CHINT current-voltage characteristics

A number of 2D CHINT simulations have been performed, varying the device geometry, transport parameters and bias conditions. Fig. 3 shows $I_D(V_{DS})$ characteristics for a single device at $T=300$K using a series of fixed collector voltages (V_{CS}). Close examination of the characteristics shows numerous topological transformations. Beginning as an accumulation mode FET at low V_{CS} (<1.0V), the onset of RST initiates the formation of a slight NDR region in the $+V_{DS}$ direction (≈ 1.0V). At higher V_{CS}, separate folds begin to appear for both $V_{DS}>0$ and $V_{DS}<0$, although the curves remain singly connected.

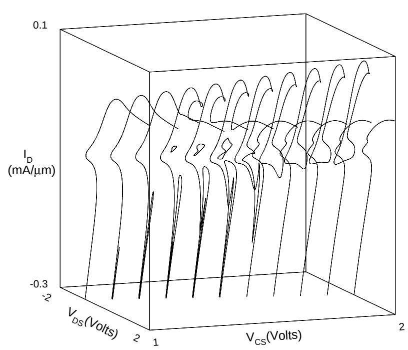

Figure 3:
CHINT I_D-V_{DS} characteristics for $1.0\text{V} \le V_{CS} \le 2.0\text{V}$ ($L_{CH}=5\mu$m, $d_B=0.2\mu$m, $v_{sat}=1\times10^7$cm / s). Curves represent simulations at constant V_{CS} separated by $\Delta V_{CS}=0.1$V.

At $V_{CS} \approx 1.2$V, a disconnected loop begins to appear in the left-hand plane, corresponding to a surface bounded by a minimum V_{CS} in the 3D space in fig. 3. As shown in fig. 4 ($V_{CS}=1.5$V), this closed loop and the needle-like fold emanating from the bottom of the left-hand plane both continue to open, and the ‘‘S-shaped’’ notch in the right-hand plane (the knee reached by tracing backwards from $V_{DS}=+\infty$) moves leftward as V_{CS} increases. By $V_{CS}=1.6$V, the characteristic is transformed into a loop which includes the origin, and a singly connected component which is multivalued but has no folds or intersections with the loop. These two components maintain essentially the same topology for larger V_{CS} although their separation in

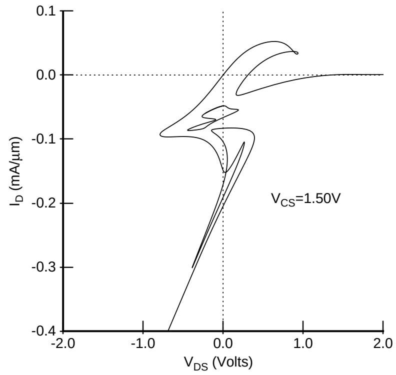

Figure 4:
Single CHINT I_D-V_{DS} characteristic from fig. 3 for $V_{CS} = 1.50$V which contains both a self-intersecting component and a disconnected loop.

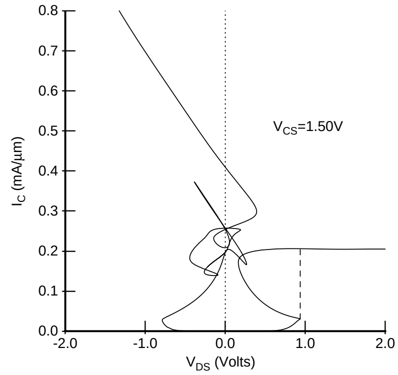

Figure 5:
Single CHINT I_C-V_{DS} characteristic for $V_{CS} = 1.50$V corresponding to the I_D-V_{DS} in fig. 4.

(I, V) increases; see fig. 6.

Note the multiplicity of anomalous $V_{DS} = 0$ states[5, 7]. A conjecture can be made that in general, at $V_{DS} = 0$, we can expect an odd number m_{S} of symmetric states and an even number m_{A} of asymmetric ones. Varying V_{CS}, we have been able to realize cases with $(m_{\mathrm{S}}, m_{\mathrm{A}}) = (1, 0)$, $(3, 0)$, $(3, 2)$, $(3, 4)$, and $(5, 4)$. It should be noted, of course, that in a continuous variation of V_{CS} one can arrive at a situation when the $I_{\mathrm{D}}(V_{DS})$ curve only touches the $V_{DS} = 0$ axis without crossing. At this singular point there is an accidental degeneracy of two symmetric states, and the total number of distinct symmetric states becomes even. With this qualification in mind, the above conjecture is based on the plausible proposition that there should always be one and only one unbounded path in the (V_{DS}, I_{D}) plane, and the symmetry requirement that asymmetric states come in pairs. Interestingly the symmetry partners may belong to topologically disconnected branches of the I_D–V_{DS} characteristic. It is in fact the existence of unpaired asymmetric states along the singly connected, outer curve in fig. 4 that has led us to the discovery[6] of the loop, disconnected from the origin.

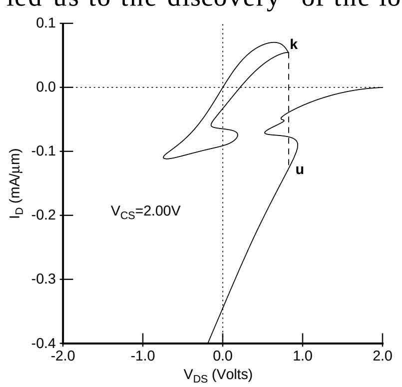

Figure 6:
Single CHINT I_D-V_{DS} characteristic from fig. 3 for $V_{CS} = 2.00$V which contains both a self-intersecting component and a disconnected loop.

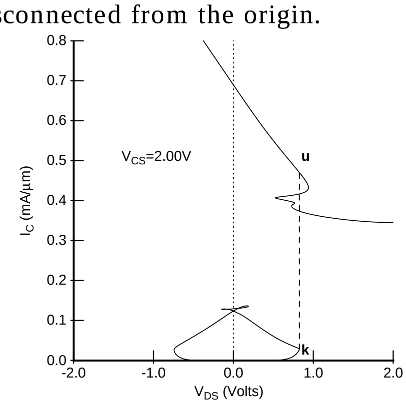

Figure 7:
Single CHINT I_C-V_{DS} characteristic for $V_{CS} = 2.00$V corresponding to the I_D-V_{DS} in fig. 4.

Figs. 5,7 show corresponding maps of the I_C-V_{DS}. With the I_D-V_{DS} plots in figs. 4,6, they completely define the device state since $I_C = I_S + I_D$. Although slices of I_C-V_{DS} space for a given V_{CS} are not symmetric, there is symmetry in the 3D space defined by $I_C(-V_{DS}, V_{CS} - V_{DS}) = I_C(V_{DS}, V_{CS})$. Points defined by a single intersection with the $V_{DS} = 0$ axis correspond to single symmetric states ($I_C = 2I_D = 2I_S$); points defined by two coincident intersections represent reflective, asymmetric pairs.

The curves in figs. 3-7 have the property that except in the vicinity of self-intersections, their infinitesimally close points correspond to infinitesimally close state vectors $\mathbf{z} \in \boldsymbol{R}$ in the multidimensional space $\boldsymbol{R}$, describing the state of the device [i.e. all the fields $n(x,y)$, $T_e(x,y)$, $\psi(x,y)$, etc.]. The converse, however, is always true: points separated by a finite distance on a (V, I) plane correspond to macroscopically distinct states $\mathbf{z}$. Continuation in the pseudo-arclength produces a completely smooth evolution of the device state. In contrast, experimental measurements (and MC simulations) force abrupt transitions at limit points, for instance $\mathbf{k} \rightarrow \mathbf{u}$ in figs. 6,7 as V_{DS} is increased from 0, corresponding to the formation or repositioning of high-field, high-temperature domains. The resultant negative I_D at $\mathbf{u}$, which has been observed experimentally[5], arises as the potential in the hot electron domains is lower than that of the drain, due to the unscreened collector field that arises from carrier depletion.

Fig. 8 shows the results of continuation simulations started from the origin for $V_{DS} > 0$, using a higher saturation velocity v_{sat}. Both the V_{CS} and V_{DS} thresholds for causing folds or limit points in IV increases with v_{sat}. As shown in fig. 9, the thresholds are reduced for smaller L_{CH}. These dependencies are similar to that for the critical ramp speed of a transient V_{CS} excitation required to induce the highest current $V_{DS} = 0$ state[5, 7].

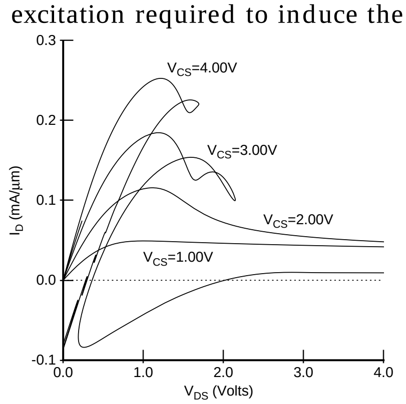

Figure 8:
CHINT I_D-V_{DS} characteristics as a function of V_{CS} ($L_{CH} = 5\mu$m, $d_B = 0.2\mu$m, $v_{sat} = 2\times10^7$cm / s). Results are shown only for the $V_{DS} > 0$ branches initiated from the origin.

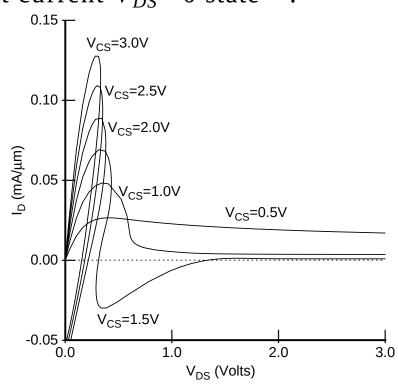

Figure 9:
CHINT I_D-V_{DS} characteristics as a function of V_{CS} ($L_{CH} = 2\mu$m, $d_B = 0.2\mu$m, $v_{sat} = 1\times10^7$cm / s). Results are shown only for the $V_{DS} > 0$ branches initiated from the origin.

In spite of the somewhat artificial $v(F)$ and $T_e(F)$ assumed for our present purposes, we believe it can be safely concluded that the cause of the nonlinear steps observed past the RST threshold in experiments are the loops and folds predicted by continuation. Transient simulations corresponding to measurement procedures indicate that folds (e.g. in fig. 8 for $V_{CS} = 3.0$V) can be followed to some length. Predictions of where the state transition will occur can be extracted accurately from complete dc IV maps, but this analysis must include consideration of NDR effects at all terminals as well as external circuit configurations.

Conclusions

Current-voltage characterizations of charge injection transistors are performed using predictor-corrector continuation methods. Simulations show the existence of multiply connected, self-intersecting *IV* curves which cannot be continuously traced in measurements or conventional simulations. The analysis suggests that it is these loops and folds that are responsible for the nonlinear steps observed after the onset of real-space transfer (RST) in experiments.

In addition to providing global information about complex switching transitions, complete *IV* mappings give reliable dc *stability* bounds, subsequently supported by more costly transient simulations. It is expected that this adaptive approach to characterization will not only be invaluable in the study of more complex RST elements[13] but also in the analysis of general, multi-terminal functional device blocks as the computational procedure requires only the size of the (V, I) domain to be mapped and a single error tolerance.

References

1. A. Kastalsky and S. Luryi, *IEEE Electron Dev. Lett.* **EDL-4**, 334 (1983); S. Luryi et al., *IEEE Trans. Electron Dev.* **ED-31**, 832 (1984).
2. P. M. Mensz et. al., *Appl. Phys. Lett.* **56**, 2563 (1990); *ibid.* **57**, 2558 (1990).
3. I. C. Kizillyalli and K. Hess, *J. Appl. Phys.* **65**, 2005 (1989).
4. W. M. Coughran, Jr. et. al., *IEEE Trans. CAD of ICs* **3**, 307 (1988); W. M. Coughran, Jr. et. al., *J. Comp. Appl. Math.* **26**, 47 (1989).
5. S. Luryi and M. R. Pinto, *Phys. Rev. Lett.* **67** (1991).
6. M. R. Pinto and S. Luryi, *1991-IEDM Technical Digest*.
7. S. Luryi and M. Pinto, this volume.
8. M. R. Pinto, in *ULSI Science and Technology*, J. Andrews and G. K. Cellar, eds., *Electrochem. Soc. Proc.* **91-11**, (1991).
9. R. Stratton, *Phys. Rev.* **126**, 2002, (1962).
10. K. Bløtekjaer, *IEEE Trans. Electron Dev.* **ED-17**, 38 (1970).
11. D. M. Caughey and R. E. Thomas, *Proc. IEEE* **55**, 2192 (1967).
12. K. Hess and C.-T. Sah, *IEEE Trans. Electron Dev.* **ED-25**, 1399 (1978); G. Baccarani and M. R. Wordeman, *Solid-St. Electron.* **28**, 407 (1985).
13. S. Luryi, et. al., *Appl. Phys. Lett.* **57**, 1787 (1990).